Empirical Determination of the Energy Loss Rate of Accelerated Electrons in a Well-Observed Solar Flare

Gabriele Torre[1], Nicola Pinamonti[1], A. Gordon Emslie[2], Jingnan Guo[1], Anna Maria Massone[3] & Michele Piana[1,3]

ABSTRACT

We present electron images of an extended solar flare source, deduced from *RHESSI* hard X-ray imaging spectroscopy data. We apply the electron continuity equation to these maps in order to determine empirically the form of the energy loss rate for the bremsstrahlung-emitting electrons. We show that this form is consistent with an energy transport model involving Coulomb collisions in a target with a temperature of about 2×10^7 K, with a continuous injection of fresh deka-keV electrons at a rate of approximately 10^{-2} electrons s^{-1} per ambient electron.

Subject headings: Sun: activity – Sun: flares – Sun: hard X-rays

1. Introduction

A substantial fraction of the energy released during the impulsive phase of a solar flare typically appears in the form of accelerated electrons. In the generally-accepted "thick-target" model (Brown 1971), these electrons are accelerated high in a coronal magnetic loop and propagate along the guiding field lines into the dense chromosphere, in which they are thermalized. As they do so, they emit bremsstrahlung hard X-ray radiation in collisions with ambient ions, resulting in a prompt, quantitative signature of the emitting electron spectrum. The accelerated electrons also lose energy through interaction with ambient particles, resulting in a variation of the emitting electron spectrum with position in the target.

[1]Dipartimento di Matematica, Università di Genova, Genova, via Dodecaneso 35 16146 Genova, Italy (torre@dima.unige.it, pinamont@dima.unige.it, guo@pitagora.dima.unige.it, piana@dima.unige.it)

[2]Department of Physics and Astronomy, Western Kentucky University, Bowling Green, KY 42101 (emslieg@wku.edu)

[3]CNR - SPIN, via Dodecaneso 33, I-16146 Genova, Italy(annamaria.massone@cnr.it)

It is widely believed that the predominant energy loss process involves inelastic collisions with ambient electrons (Brown 1972; Lin & Hudson 1976; Emslie 1978), although other processes, such as return current ohmic losses (e.g., Knight & Sturrock 1977; Emslie 1980; Zharkova & Gordovskyy 2006) and wave-particle interactions (e.g., Hoyng & Melrose 1977; Hannah & Kontar 2011), may, under certain conditions, also play an important role. The oft-used collisional cold-target energy loss formula (e.g., Emslie 1978) has an associated spatial energy loss rate dE/ds that varies with energy according to $1/E$. However, in a warm target the actual energy loss rate involves the temperature T of the ambient medium (Spitzer 1962; Frankel 1965). For energies of the order of kT, where k is Boltzmann's constant, the correction terms to the cold-target formula can be significant.

The Ramaty High Energy Solar Spectroscopic Imager (*RHESSI* ; Lin et al. 2002) has gathered spatially and spectrally resolved hard X-ray data with angular resolutions down to a few arcseconds and spectral resolution of order 1 keV. Piana et al. (2007) have shown how to use hard X-ray imaging spectroscopy data from *RHESSI* to construct maps of the mean *electron* flux $\overline{F}(x, y; E)$ (weighted by the line-of-sight column density at the point in question in the image plane) at many different electron energies E. Because the basic way in which *RHESSI* records imaging information – as temporal modulation of flux induced by the rotation of occulting grids in front of the detectors – the spatial information is contained not in pixel-by-pixel form, but rather in two-dimensional spatial Fourier components ("visibilities") of the count-based image in the plane of the sky. Hence, the essence of the method used to construct the electron maps involves regularized spectral inversion of the measured count visibilities to produce electron visibilities. Standard Fourier-transform-based image reconstruction algorithms may then be used to convert these visibility values into maps of the electron flux spectrum.

Such maps are very useful in visualizing the variation of the electron spectrum throughout the source. They also afford the intriguing possibility (Emslie, Barrett, & Brown 2001) of actually measuring the variation of the emitting electron spectrum with position in the target and so, through the electron continuity equation, determining quantitative information on the form of the variation of electron energy loss rate with energy. This form can then be compared with the formulae appropriate to various candidate energy transport mechanisms (e.g., Coulomb collisions) in order to assess the viability of the candidate energy transport process. In the present paper, we illustrate the application of just such a methodology to the extended coronal event of 2002 April 15.

In Section 2 we review the essential elements of the process through which electron maps are reconstructed from *RHESSI* count visibilities. In Section 3 we present the standard continuity equation for the electron flux spectrum $F(x, y, z; E)$. We also show how this

can, under plausible assumptions, be used to generate a continuity equation for the column-density-weighted averaged electron distribution function $g(E,s) = N(s)\,\overline{F}(E,s)$, a quantity that can be directly inferred from observations of the hard X-ray count spectrum $I(x,y;q)$ at points (x,y) lying along a one-dimensional locus s in the image plane. In Section 4 we apply this continuity equation to electron maps constructed for the coronal source in the 2002 April 15 event to derive empirically the variation of the energy loss rate dE/ds with energy E. In Section 5, these results are compared with the formula for Coulomb collisions in a warm target, and it is noted that an acceptable fit is obtained only if allowance is made for injection of freshly-accelerated electrons throughout the source. In Section 6 we assess the values of the target density and the injection (source) term thus obtained.

2. *RHESSI* visibilities and electron maps

As shown in Equation (A3) of Piana et al. (2007), the relation between the mean electron flux spectrum $\overline{F}(x,y;E)$ (electrons cm^{-2} s^{-1} keV^{-1}), averaged over the line-of-sight distance z through the point (x,y,z) in a target, and the corresponding hard X-ray spectrum $I(x,y;\epsilon)$ (photons cm^{-2} s^{-1} keV^{-1} arcsec^{-2}) emitted per unit area of the source is

$$I(x,y;\epsilon) = \frac{a^2}{4\pi R^2}\int_{E=\epsilon}^{\infty} N(x,y)\,\overline{F}(x,y;E)\,Q(\epsilon,E)\,dE, \tag{1}$$

where $a = 7.25\times10^7$ cm arcsec^{-1} at $R = 1$ AU, $Q(\epsilon,E)$ (cm^2 keV^{-1}) is the bremsstrahlung cross-section differential in electron energy E and $N(x,y)$ (cm^{-2}) is the column density along the line of sight.

RHESSI's nine Rotating Modulation Collimators (RMCs) provide count-based visibility (i.e., spatial Fourier component) information at a series of points distributed over nine circles in the spatial frequency (u,v) plane. We define the *count visibility spectrum* $V(u,v;q)$ (counts cm^{-2} s^{-1} keV^{-1}) as the two-dimensional spatial Fourier transform of the count spectrum image $J(x,y;q)$ (counts cm^{-2} s^{-1} keV^{-1} arcsec^{-2}) at count energy q (keV), and the *electron visibility spectrum* $W(u,v;E)$ as the two-dimensional spatial Fourier transform of the column-density-weighted mean electron flux image $N(x,y)\,\overline{F}(x,y;E)$. Then, with $D(q,\epsilon)$ as the (dimensionless) differential element of the detector response matrix, Piana et al. (2007) showed – their equation (A9) – that the relation between the observed count visibilities and the electron flux visibility spectra is

$$V(u,v;q) = \frac{1}{4\pi R^2}\int_{q}^{\infty} W(u,v;E)\,K(q,E)\,dE, \tag{2}$$

where the kernel $K(q, E)$ satisfies

$$K(q, E)\, dq = \int_{\epsilon=q}^{\infty} D(q, \epsilon)\, Q(\epsilon, E)\, d\epsilon; \tag{3}$$

i.e., is a convolution of the detector response matrix with the bremsstrahlung cross-section.

The essential *RHESSI* imaging spectroscopy problem is to reconstruct maps of $\overline{F}(x, y; E)$ at different electron energies E from observed *RHESSI* count visibilities $V(u, v; q)$. As described in Piana et al. (2007), the most effective method do accomplish this is to first invert equation (2) using a regularized spectral inverse operation to arrive at the electron visibilities $W(u, v; E)$. Various techniques can then be used to use this Fourier transform data to construct images of the electron flux, and it should be noted that through this process it is possible to produce electron maps at energies E higher than the highest input count energy $q_{\max}$. Since the regularization process effectively introduces a smoothing constraint across electron energies, the resulting electron visibility sets (and so maps) vary smoothly from one electron energy channel to the next. This in turn allows the construction of electron spectra that vary smoothly with spatial location, permitting an empirical analysis of energy loss processes to be carried out.

3. The Electron Continuity Equation

The electron flux continuity equation, expressed in terms of electron energy E along a direction s, may be written (e.g, Emslie, Barrett, & Brown 2001)

$$\frac{\partial F(E, s)}{\partial s} + \frac{\partial}{\partial E}\left(F(E, s)\,\frac{dE}{ds}\right) = S(E, s), \tag{4}$$

where $F(E, s)$ (electrons cm^{-2} s^{-1} keV^{-1}) is the electron flux, differential in energy, and $S(E, s)$ (electrons cm^{-3} s^{-1} keV^{-1}) is a source term.

It must be noted that $F(E, s)$ cannot be directly inferred from observations at this time. However, if we assume that $F(x, y, z; E) = \overline{F}(x, y; E)$ (i.e., that the electron flux spectrum is independent of the position along the line-of-sight) and also impose the condition

$$\left|\frac{dN(s)}{ds}\, F(E, s)\right| \ll \left|N(s)\frac{\partial F(E, s)}{\partial s}\right|, \tag{5}$$

then equation (4) is readily transformed into

$$\frac{\partial g(E,s)}{\partial s} + \frac{\partial}{\partial E}\left(g(E,s)\,\frac{dE}{ds}\right) = h(E,s), \tag{6}$$

where $g(E,s) = N(s)\,\overline{F}(E,s)$ (electrons cm^{-4} s^{-1} keV^{-1}) is the quantity represented in observationally-deduced electron maps and $h(E,s) = N(s)\,S(E,s)$ (electrons cm^{-5} s^{-1} keV^{-1}) is the line-of-sight-column-density-weighted source term. We can solve equation (6) for the energy loss rate

$$\frac{dE}{ds}(E,s) = \frac{1}{g(E,s)}\int_E^\infty \left[\frac{\partial g(E,s)}{\partial s} - h(E,s)\right] dE \ , \tag{7}$$

which is a function of both electron energy E and position s. Here we have assumed that the energy loss process is such that energy loss is negligible at high energies: $dE/ds \to 0$ as $E \to \infty$.

At this point, a few remarks concerning the assumption (5) are in order. This condition is equivalent to

$$\left|\frac{d\ln N(s)}{ds}\right| \ll \left|\frac{\partial \ln F(E,s)}{\partial s}\right|, \tag{8}$$

which essentially requires that the spatial variation of the electron spectrum $F(E,s)$ is more significant than the spatial variation of the line-of-sight column density $N(s)$ in determining the variation of the product $N(s)\,F(E,s)$. For an exponential atmospheric model with scale height H, $d\ln N(s)/ds = 1/H$ and so condition (8) is equivalent to $1/H \ll |\partial \ln F/\partial s|$. For Coulomb collisions in a cold target, $|dE/ds| \sim Kn/E$. The characteristic stopping distance for an electron of energy E is thus $s \sim E^2/2Kn$, so that $|\partial \ln F/\partial s| \simeq 2Kn/E^2$. Condition (8) is thus equivalent to the relation $E^2/2Kn \ll H$; substituting numerical values gives $[E(\mathrm{keV})]^2 \ll 10^{-17}\,n(\mathrm{cm}^{-3})H(\mathrm{cm})$. Taking $n \simeq 10^{11}$ cm^{-3} as a plausible density (this is *a posteriori* consistent with the empirical value to be determined in Section 5 below), this condition becomes $E^2 \ll 10^{-6}H$. Finally, since the hard X-ray brightness (and so the line-of-sight column density) is observed to vary only slightly along the loop length, we set a lower limit on the scale height as the length of the loop: $H > 10^{10}$ cm. With this value, condition (8) certainly holds for electron energies smaller than ~ 100 keV and so for the deka-keV electron energies under consideration.

4. Application to observations

As a preliminary, we rearrange equation (7) into the form

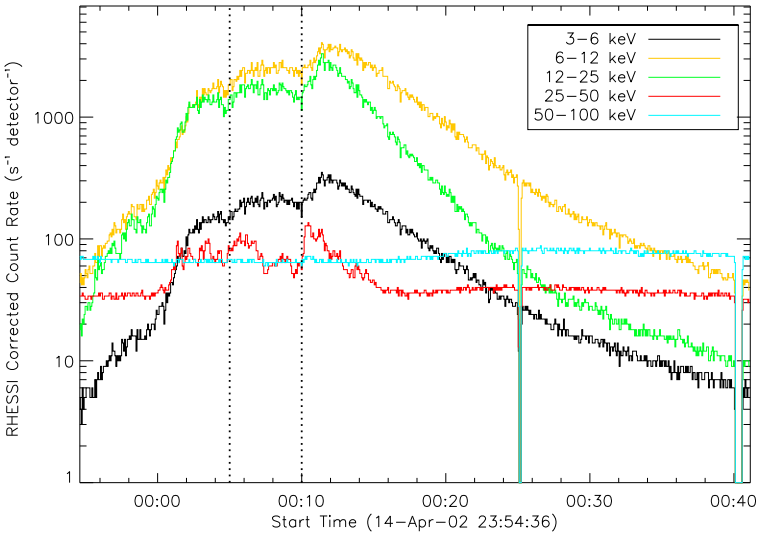

Fig. 1.— *RHESSI* hard X-ray lightcurves of the 2002 April 15 event in each of five energy channels.

$$R(E,s) \equiv -\frac{dE}{ds}(E,s) - \frac{1}{g(E,s)}\int_E^\infty h(E,s)\,dE = -\frac{1}{g(E,s)}\int_E^\infty \frac{\partial g(E,s)}{\partial s}\,dE \quad , \qquad (9)$$

a form which results in the right-hand side being a directly measurable quantity.

Inserting the inferred values of $g(E,s)$ in the right-hand side of equation (9), we calculated the values of $R(E,s)$ for the flaring loop structure that is the predominant feature in the 2002 April 15 00:05 - 00:10 UT event. This event has been studied by numerous authors (Sui et al. 2004; Veronig & Brown 2004; Bone et al. 2007; Xu et al. 2008; Kontar et al. 2011). The time interval used is highlighted in Figure 1. Figure 2 shows the corresponding electron maps, in 2 keV energy channels covering the energy range from 12 to 36 keV.

To determine the direction defining the spatial variable s, we selected a locus of points by the following means. For each image, we

1. applied a mask to select only pixels with intensity larger than 10% of the maximum of the whole map;

2. selected a row in the image (i.e., a specific y value in the image plane), and searched for the pixel with maximum intensity in that row; and

3. repeated this procedure for each pixel row in order to determine the locus of maximal intensity, which we take to define the guiding magnetic field line along which the electrons propagate.

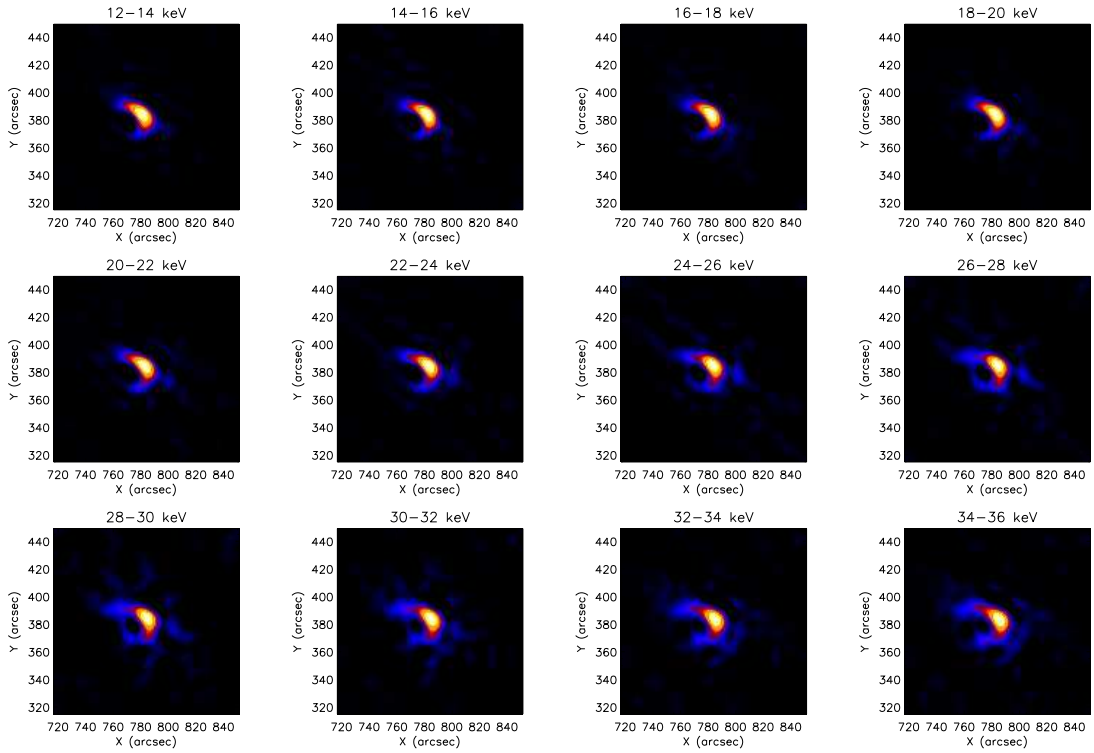

Fig. 2.— Electron maps for the 2002 April 15 event. From left to right along each row, and from top to bottom, the images are for the energy bands 12-14 keV, 14-16 keV, $\cdots$, 34-36 keV, respectively.

An example of this procedure, for the (12-14) keV map, is shown in Figure 3, where we utilized pixel rows from $y = 369$ arcsec to $y = 394$ arcsec. To verify the robustness of this technique, we rotated the cooordinate system by various angles and repeated the analysis. Because of the orientation of the magnetic loop in this particular event, application of this analysis at angles greater than about $\sim 20^\circ$ results in a given row of pixels intercepting the maximum intensity locus more than once[4]. However, for all angles up to $\sim 20^\circ$, the same locus of brightest points was obtained.

[4]In general, searching for the location of the loop axis by this technique will require general consideration of the orientation of the loop, to ensure that each row intersects the loop axis only once.

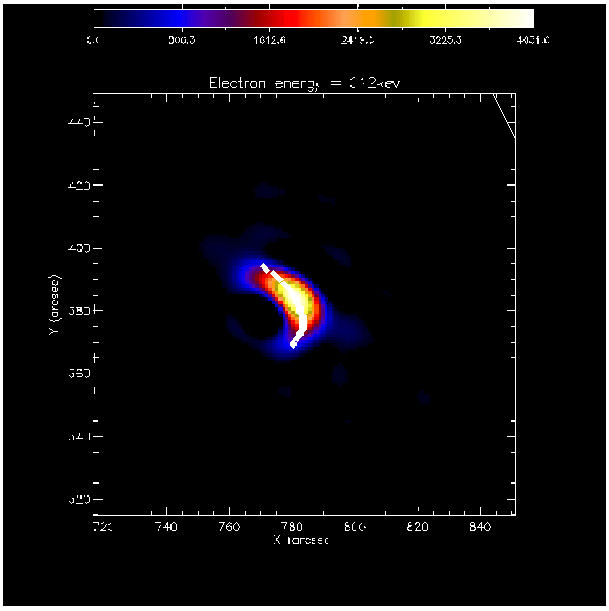

Fig. 3.— Output of the image processing procedure that provides points that specify the direction of the guiding magnetic field axis of the loop. Here we have superimposed such points as a white line on the 12-14 keV image.

To evaluate $R(E, s)$, the spatial gradients $\partial g(E, s)/\partial s$ for each electron energy channel, and at each point along the selected locus in Figure 3, were calculated using simple first-order, centered, numerical differentiation. To define the direction s, we used the locus of brightest points in the (12-14) keV energy band[5]. Although, due to spectral variations, this particular set of points may not always be the locus of the brightest points in the image for each energy channel, it is, of course, important to use the same locus of points in computing spatial variations in the electron spectrum $g(E, s)$. The energy integral on the right side of equation (9) was evaluated using simple trapezoidal integration, with the upper integral limit set at $E = 72$ keV, the highest energy at which a reliable image could be obtained.

Results of this procedure are shown in Figure 4, where each panel represents the value of $R(E, s)$ (in units of keV arcsec^{-1}) as a function of position in the loop, at the energy specified above the plot in question. Results are shown for electron energies from 12 keV to 32 keV (lower energy value of the 2 keV bin); above this range the electron visibilities used to construct the electron maps begin to significantly deteriorate, so that the electron

[5]The choice of the (12-14) keV image as the reference is arbitrary; however, the results of the paper are not substantially changed if a different reference energy band is chosen.

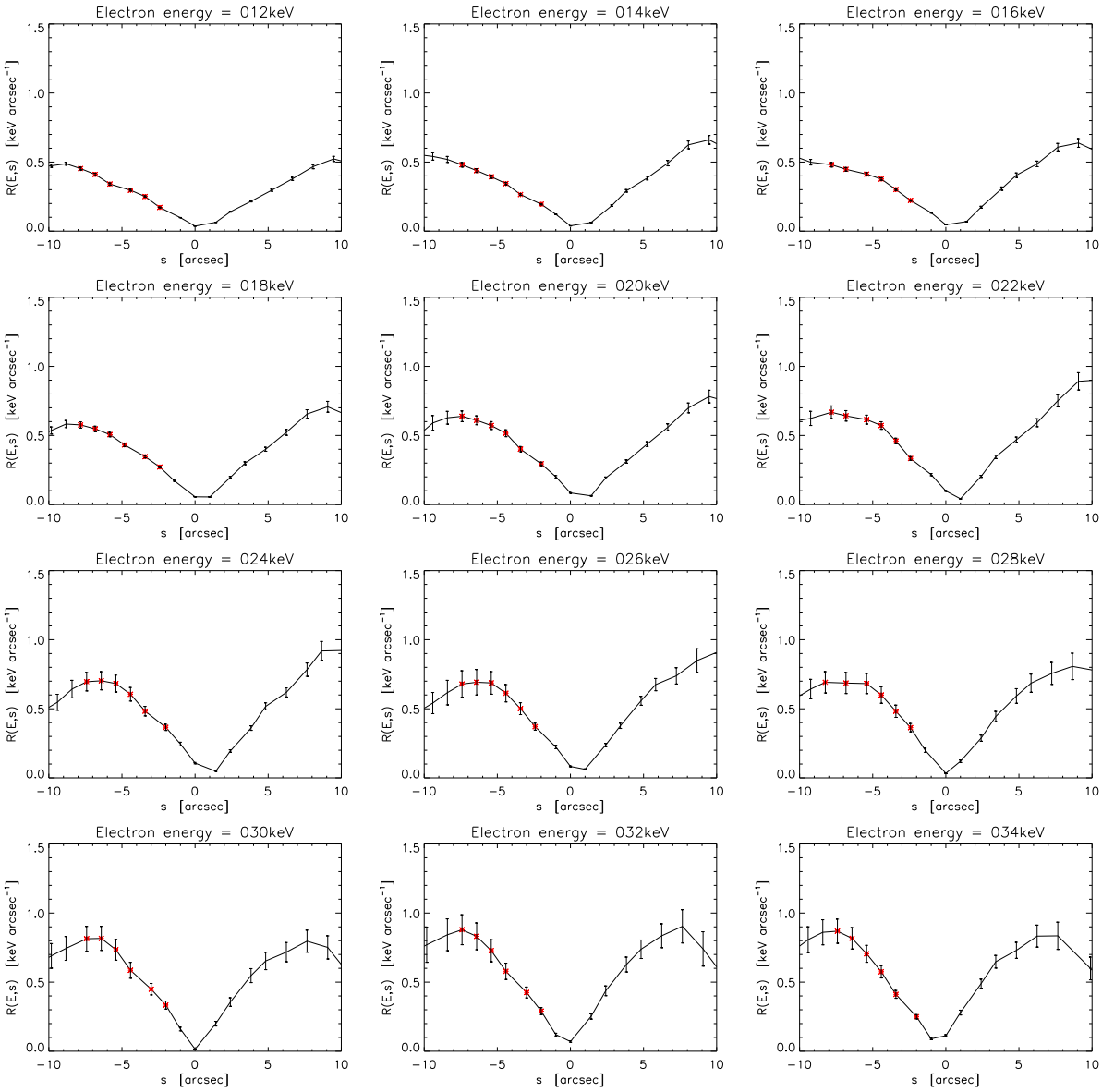

Fig. 4.— $R(E, s)$ (see equation [9]) as a function of position s in the magnetic guiding line for the same energy channels considered in Figure 2. The six points used to compute the value of $R(E)$ used in subsequent analysis have been highlighted in red.

images become unusable. The position of the minimum value in these plots is very stable around the position of the maximum emission, i.e., $x = 780$ arcsec, $y = 384$ arcsec, which we interpret as a clear signature of the position of the center of the injection region (see below).

To improve the statistics, we performed averages of $R(E, s)$ over the six positions highlighted in red in all panels of Figure 4. The values $R(E)$ of these spatially-averaged values are shown in Figure 5; the error bars on the points were determined using a Monte Carlo procedure in which the input count visibility sets were randomly perturbed and the calculation repeated.

5. Interpretation of results

These results can now be used to study the behavior both of the electron energy loss rate as a function of energy, and of the source function $h(E)$.

Most frequently used theoretical models for the energy loss rate are based on Coulomb collisions. In the case of a cold target, this model predicts

$$\frac{dE}{ds} = -\frac{K\, n(s)}{\mu\mu' E} \quad , \tag{10}$$

where E (keV) is the electron energy, s the distance (cm) in the plane of the sky, μ is the cosine of the average pitch angle (the angle between the electron trajectory and the magnetic field line), μ' is the cosine of the projection angle between the distance in the plane of the sky and the physical distance on the Sun, and $K = 2\pi e^4 \Lambda = 2.8 \times 10^{-18}$ cm^2 keV^2 (e being the electronic charge and Λ the Coulomb logarithm). This monotonically decreasing form is clearly inconsistent with the data-derived form of $R(E)$ shown in Figure 5. We believe that this is due to two main reasons:

1. First, the finite temperature of the target. For this event, a Maxwellian (isothermal) fit to the spatially-integrated hard X-ray spectrum yielded an emission measure of 7.6×10^{48} cm^{-3} and a temperature of 1.61 keV. For such an ambient temperature, the velocities of the ~ 20 keV electrons under consideration are only about $3 - 4$ times the thermal velocity, so that the warm-target correction is significant in the computation of the energy loss rate;

2. Second, the presence of the source term $h(E, s)$ appearing in the formula for $R(E, s)$. Xu et al. (2008) have shown that the size of the acceleration region in this event is a

significant portion of the whole emitting region, which implies that that the assumption of point-wise injection is not realistic.

In order to evaluate the influence of the thermal effects onto the collisional model predicting the energy loss rate, we adopt the formula given by Spitzer (1962) (see also Emslie 2003)

$$\frac{dE}{ds} = -\frac{Kn}{\mu\mu' E}\left[\mathrm{Erf}\left(\sqrt{\frac{E}{kT}}\right) - \frac{4}{\sqrt{\pi}}\sqrt{\frac{E}{kT}}\,e^{-E/kT}\right], \tag{11}$$

where Erf is the error function. Furthermore, we included a source term in equation (9) with the form

$$h(E,s) = \begin{cases} h_0\left(\frac{E}{E_0}\right)^{-\delta}; & |\,s| \le \frac{L_0}{2} \\ 0; & |\,s| > \frac{L_0}{2} \end{cases}, \tag{12}$$

where δ is the spectral index of the injected electron spectrum and L_0 is the half-length of the acceleration region. This form is motivated by the work of Xu et al. (2008), Kontar et al. (2011) and Guo et al. (2012), who have shown that extended coronal sources such as that considered here are often characterized by a variation of length $L(E)$ that is consistent with an acceleration region of finite length L_0 coupled to an exterior "propagation" region. The value of δ is obtained from spectral fitting of the power-law part of the spatially-integrated hard X-ray spectrum, yielding $\delta = \gamma + 1 = 9.9 \pm 0.1$.

We fitted the same six-position-averaged data in Figure 5 with a functional form representing the left-hand side of equation (9). We took dE/ds to be of the form (11), with $kT = 1.61$ keV, and the form of the integral in the second term on the left-hand side was deduced from the form (12), namely

$$\int_E^\infty h(E,s)\,dE = \begin{cases} \frac{h_0\,E}{(\delta-1)}\left(\frac{E}{E_0}\right)^{-\delta}; & |\,s| \le \frac{L_0}{2} \\ 0; & |\,s| > \frac{L_0}{2} \end{cases}, \tag{13}$$

with the reference energy E_0 set arbitrarily at 20 keV. The best-fit profiles for values $L_0 = 0, 10''$, and $16''$ are shown[6]. The fit for the point-source injection model ($L_0 = 0$; dot-dashed

[6]Note that, unlike the dot-dashed curve corresponding to the point-source injection case $h = 0$, the dashed and solid lines corresponding to finite values of L_0 (and hence h) are not perfectly smooth. This is because of the discretely observed values of $g(E,s)$ that appear in the denominator of the second term on the left side of equation (9).

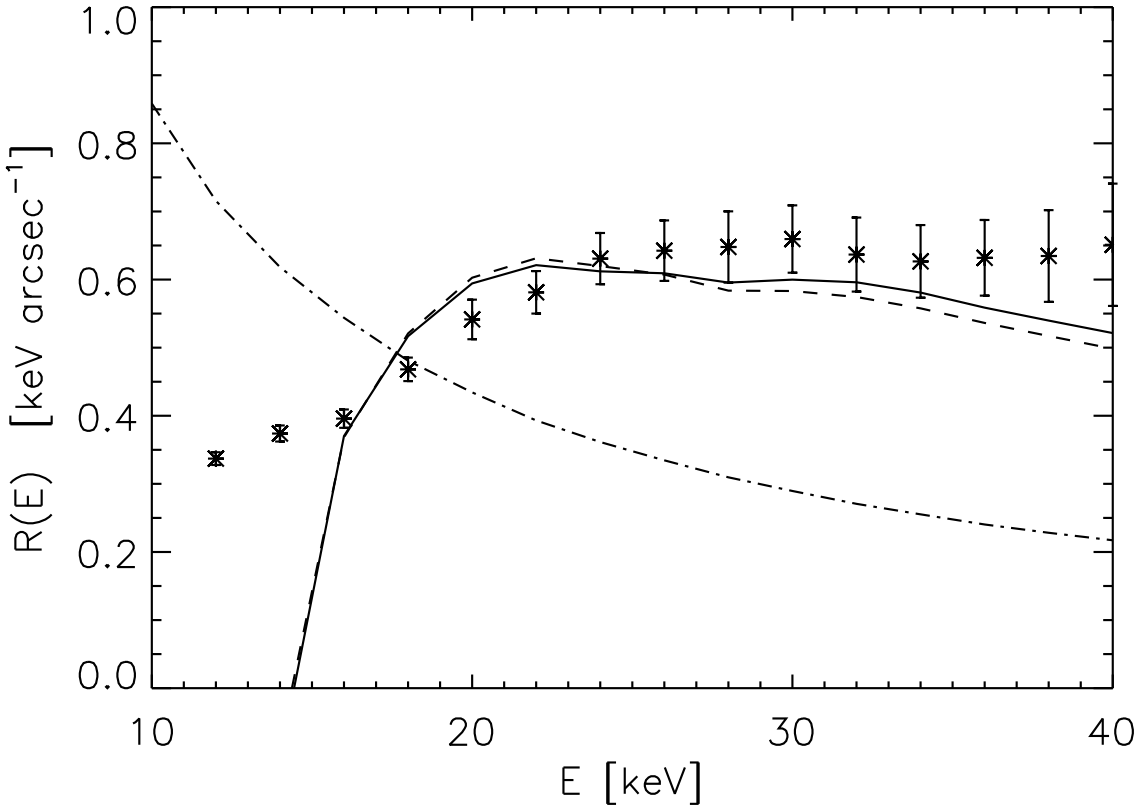

Fig. 5.— $R(E)$, averaged over the six positions highlighted in Figure 4, as a function of electron energy E. The dot-dashed, dashed, and solid lines correspond to fits of the theoretical model of equation (9) to the data, with temperature $T = 1.61$ keV and acceleration region length $L_0 = 0, 10$, and 16 arcseconds, respectively.

line in Figure 5) is clearly unacceptable ($\chi^2 = 47.6$), indicating that a point-source injection model cannot account for the observations: continuous injection of fresh electrons along the length of the source is a key ingredient in explaining the observed behavior of $R(E)$. The value of χ^2 generally decreases as L_0 is increased. More acceptable fits ($\chi^2 \sim 3.5$) result from setting $L_0 = 5'' - 10''$ (see dashed curve for $L_0 = 10''$ in Figure 5), and the data are best matched ($\chi^2 = 2.1$) by setting $L_0 = 16''$ (see solid curve in Figure 5), indicating that acceleration occurs over most of the observable emitting region. Such a value of L_0 is remarkably consistent with the value $(16 \pm 1)''$ found by Guo et al. (2012) in an independent analysis of the same event, in which the variation of source size with electron energy E was studied.

The best-fit target density straightforwardly scales (see equation [11]) linearly on both the pitch-angle cosine μ and the projection-angle cosine μ'; for $\mu = \mu' = 1$ and $L_0 = 16''$, it is $n = (2.0 \pm 0.1) \times 10^{11}$ cm^{-3} (with proportionately smaller values if we adopt values of μ and μ' that are < 1). Based on the geometry of the flare in question, we believe that $\mu' = 1$ is a reasonable approximation (i.e., that projection effects related to the angle between the guiding field line and the plane of the sky are negligible); however, the reasonableness of this assumption may be called into question if the guiding magnetic field has a substantial degree of helical twist. And, we know relatively little about the value of μ, which depends on the angular distribution of the accelerated particles.

The best-fit injection rate (weighted by the line-of-sight column density) is $h_0 = (1.4 \pm 0.1) \times 10^{28}$ cm^{-5} keV^{-1} s^{-1}, a quantity that is independent of μ and μ'. The magnitude of this source term provides important information on particle acceleration processes. Following Emslie et al. (2008), we define the *specific acceleration rate* (above reference energy E_0) as

$$\eta(E_0) = \frac{1}{\mathcal{N}} \frac{d\mathcal{N}}{dt}, \tag{14}$$

where $\mathcal{N}$ is the number of electrons in the acceleration region and $d\mathcal{N}/dt$ is the rate of acceleration of electrons to energies of E_0 or above. Assuming a homogeneous source term, an equivalent expression for $\eta(E_0)$ can be obtained by dividing the acceleration rate per unit volume above energy E_0 by the ambient density n. This gives

$$\eta(E_0) \simeq \frac{1}{n\,N} \int_{E_0}^{\infty} h\left(E, s < \frac{L_0}{2}\right) dE = \frac{1}{n\,N} \frac{h_0\,E_0}{(\delta - 1)}, \tag{15}$$

where we have used the form (12) for $h(E)$. Finally, writing the source emission measure in the form $EM = \int n^2\,dV = A \int n^2\,dz = A\,n\,N$ (where z is the direction along the line of sight), this can be written

$$\eta(E_0) \simeq \frac{A}{EM}\,\frac{h_0\,E_0}{(\delta-1)}. \tag{16}$$

Setting $E_0 = 20$ keV and the observed values $\delta = 9.9, A \simeq 500$ arcsec$^2 \simeq 2.5\times10^{18}$ cm$^2, h_0 = 1.4\times10^{28}$ cm^{-5} keV^{-1} s^{-1} and $EM = 7.6\times10^{48}$ cm^{-3}, we obtain $\eta\,(20\,\mathrm{keV}) \simeq 1.1\times10^{-2}$ s^{-1}.

6. Summary and Conclusions

We have used *RHESSI* hard X-ray imaging spectroscopy data to derive the form of the electron spectrum with position in the extended loop source of the 2002 April 15 solar flare. These results were then used to determine *empirically* the rate of change of energy with position appropriate to the electrons as they propagate throughout the bremsstrahlung source. The form of energy loss rate obtained is *not* consistent with the oft-used (e.g., Brown 1971; Emslie 1978) energy loss rate appropriate to a collisional cold target and a point-source injection. However, it *is* consistent with that for electrons suffering Coulomb collisions in an ionized hydrogen target with a finite temperature T, provided that one also allows for continuous injection of fresh electrons along most of the length of the source.

Fitting of the empirical form of the spatially averaged quantity $R(E)$ (equation [9]) yields values of the acceleration region length L_0, the target density n, and the electron injection rate per unit volume. The value of L_0 obtained is consistent with that obtained by Guo et al. (2012) in an independent analysis of the same event. The density value obtained ($n \lesssim 2\times10^{11}$ cm^{-3}, the exact value depending on the average value of the pitch angle cosine μ) is consistent with estimates of the density obtained from considerations of the source emission measure: $n = \sqrt{EM/V} \simeq \sqrt{EM/A^{3/2}}$.

The magnitude of the source term yields a specific acceleration rate $\eta \simeq 10^{-2}$ electron s^{-1} per ambient electron, independent of projection factors. Such a value of η is within the range of specific acceleration rates reported for other extended events by Emslie et al. (2008), based on the Xu et al. (2008) analysis of variation of source size with photon energy. As discussed by Emslie et al. (2008), the value of the specific acceleration rate places very substantial constraints on particle acceleration models. Further, a specific acceleration rate of the magnitude found for this event requires that replenishment of the acceleration region occur on a timescale $\tau \simeq \eta^{-1} \simeq 100$ s. Given that the event in question extended over a significantly longer period (see Figure 1), this poses significant challenges for global electrodynamic models (e.g., Emslie & Hénoux 1995) of the flare environment.

We thank the referee for some very helpful and constructive comments on an earlier ver-

sion of the manuscript, in particular for pointing out the need to consider the two projection factors μ and μ' and for suggesting a generalization of the spatial form of the injection profile. AGE was supported by NASA Grant NNX10AT78J; AMM, NP and MP were supported by the European Community Framework Programme 7, "High Energy Solar Physics Data in Europe (HESPE)," Grant Agreement No. 263086.

REFERENCES

Bone, L., Brown, J. C., Fletcher, L., Veronig, A., & White, S. 2007, A&A, 446, 339

Brown, J. C. 1971, Sol. Phys., 18, 489

Brown, J. C. 1972, Sol. Phys., 26, 441

Emslie, A. G. 1978, ApJ, 224, 241

Emslie, A. G. 1980, ApJ, 235, 1055

Emslie, A. G., 2003, ApJ, 595, L119

Emslie, A. G., Barrett, R. K., & Brown, J. C. 2001, ApJ, 557, 921

Emslie, A. G., & Hénoux, J.-C. 1995, ApJ, 446, 371

Emslie, A. G., Hurford, G. J., Kontar, E. P., Massone, A. M., Piana, M., Prato, M., & Xu, Y. 2008, in *Particle Acceleration and Transport in the Heliosphere and Beyond*, 7th Annual International Astrophysics Conference. AIP Conference Proceedings, 1039, 3

Frankel, N. E. 1965, Plasma Phys. 7, 225

Guo, J., Emslie, A. G., Kontar, E. P., Benvenuto, F., Massone, A. M., & Piana, M. 2012, A&A, submitted.

Hannah, I. G., & Kontar, E. P. 2011, A&A, 529, 109

Hoyng, P., & Melrose, D. B. 1977, ApJ, 218, 866

Knight, J. W., & Sturrock, P. A. 1977, ApJ, 217, 306

Kontar, E. P., Hannah, I. G., & Bian, N. H. 2011, ApJ, 730, L22

Lin, R. P., et al. 2002, Sol. Phys., 210, 3

Lin, R. P., & Hudson, H. S. 1976, Sol. Phys., 50, 153

Piana, M., Massone, A. M., Hurford, G. J., Prato, M., Emslie, A. G., Kontar, E. P. and Schwartz, R. A. 2007, ApJ, 665, 846

Spitzer, L., Jr. 1962, Physics of Fully Ionized Gases (New York: Interscience)

Sui, L., Holman, G. D., & Dennis, B. R. 2004, ApJ, 612, 546

Veronig, A. M., & Brown, J. C. 2004, ApJ, 603, L117

Xu, Y., Emslie, A. G., & Hurford, G. J. 2008, ApJ, 673, 576

Zharkova, V. V., & Gordovskyy, M. 2006, ApJ, 651, 553